



# Plasma-assisted dry reforming of methane over Mo<sub>2</sub>C-Ni/Al<sub>2</sub>O<sub>3</sub> catalysts: Effects of β-Mo<sub>2</sub>C promoter

Yanan Diao, Xiao Zhang, Yang Liu, Bingbing Chen, Guohao Wu, Chuan Shi \*

State Key Laboratory of Fine Chemicals, School of Chemical Engineering, Dalian University of Technology, Dalian 116024, China

## ARTICLE INFO

### Keywords:

β-Mo<sub>2</sub>C  
Ni/Al<sub>2</sub>O<sub>3</sub>  
Plasma  
DRM reaction

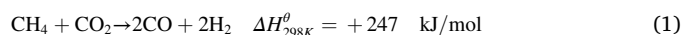
## ABSTRACT

Non-thermal plasma (NTP) coupled with catalysis provides a way to enable the dry reforming of methane (DRM) reaction to occur at low temperatures. While assistance of NTP brings the negative issue of coke deposition due to the faster rate of CH<sub>4</sub> dissociation induced by NTP. Herein, β-Mo<sub>2</sub>C was employed as an effective component to activate CO<sub>2</sub> and collaborated with Ni/γ-Al<sub>2</sub>O<sub>3</sub> for the plasma-assisted DRM reaction. Addition of β-Mo<sub>2</sub>C facilitated the charge deposition, and Ni nanoparticles were found to re-disperse over the β-Mo<sub>2</sub>C surface due to the strong interaction between Ni and β-Mo<sub>2</sub>C. Benefiting from the new active interface of Ni-Mo<sub>2</sub>C, the mechanically mixed Mo<sub>2</sub>C-Ni/Al<sub>2</sub>O<sub>3</sub> catalyst exhibited much better activity and stability as compared with the undoped Ni/Al<sub>2</sub>O<sub>3</sub> catalyst. The present study reveals the crucial roles of β-Mo<sub>2</sub>C additives, providing practical solutions to depress carbon deposition, and thereby enhance the catalytic stability in plasma-assisted DRM reaction.

## 1. Introduction

Methane (CH<sub>4</sub>) and carbon dioxide (CO<sub>2</sub>) are two of the main abundant greenhouse gases, and extensive emission of them has the key contributions in global warming. Utilization of the two abundant greenhouse gases (CH<sub>4</sub> and CO<sub>2</sub>) by dry reforming of methane (DRM) offers a valuable environmental and economic route of converting greenhouse gases to producing syngas (Eq. (1)), which is further used to synthesize oxygenated fuels and long chain hydrocarbons via Fischer-Tropsch synthesis [1,2].

From thermodynamics point of view, dry reforming of methane is an endothermic reaction, and it operates at high temperatures (typically above 700 °C) to obtain considerable conversions of CH<sub>4</sub> and CO<sub>2</sub>. Among the catalysts being employed for the DRM reaction, Ni-based catalysts are the most promising ones. While they suffer from sintering and coke deposition at high operating temperatures [3,4]. Strategies such as adding a second metal to form alloys, promoting the basicity of supports to enhance CO<sub>2</sub> adsorption and constructing a core-shell structure to restrict the sintering of Ni particles [5,6] have been widely investigated and made some progress.



Alternatively, non-thermal plasma (NTP) represents an efficient

supplementary to thermal catalysis to low down the reaction temperatures and especially enable a thermodynamic-limited reaction to occur with fast reaction rate at low temperatures. The typical electron energy (1–10 eV) generated in dielectric barrier discharge (DBD), which is effective to break C–H bond (4.5 eV) and C=O bond (5.5 eV), coupling of DBD with catalysis therefore provides a promising solution to DRM reaction to achieve high reaction rates and selectivity to C<sub>2</sub> products at lower temperatures [7]. In this connection, the sintering of Ni nanoparticles (NPs) at high operating temperatures should be relieved in NTP-assisted catalysis conditions.

Various catalysts have been investigated for the plasma-assisted DRM reaction to improve the conversion of reactants and the selectivity of main products. Among these catalysts, Ni as active metal and Al<sub>2</sub>O<sub>3</sub> as support are the most commonly studied [8–12]. Tu et al. investigated the effect of different supports (Al<sub>2</sub>O<sub>3</sub>, MgO, SiO<sub>2</sub>, TiO<sub>2</sub>) in plasma-catalytic DRM reaction. The results revealed that the highest CH<sub>4</sub> conversion (44.1%) & CO<sub>2</sub> conversion (26.2%) and the lowest surface carbon deposition of 3.8% obtained with Ni/Al<sub>2</sub>O<sub>3</sub> catalyst, which was due to higher Ni dispersion and stronger basic sites of Al<sub>2</sub>O<sub>3</sub> [13]. Additionally, some specially designed Ni-based catalysts modified by promoters of K, Mg or Ce have shown some specific properties in the plasma-catalytic DRM reaction. For example, compared to un-promoted Ni/Al<sub>2</sub>O<sub>3</sub> catalyst, adding K as a promoter increased the conversion of

\* Corresponding author.

E-mail address: [chuanshi@dlut.edu.cn](mailto:chuanshi@dlut.edu.cn) (C. Shi).

<https://doi.org/10.1016/j.apcatb.2021.120779>

Received 30 July 2021; Received in revised form 23 September 2021; Accepted 27 September 2021

Available online 4 October 2021

0926-3373/© 2021 Elsevier B.V. All rights reserved.

reactants as well as the selectivity of  $H_2$ , CO and the energy efficiency of the plasma process [14].

It is noted that the conversions of  $CO_2$  are generally higher than that of  $CH_4$  in catalysis-only conditions due to the side reaction of RWGS coupled with DRM [15–17]. While  $CH_4$  conversions are found to be higher than  $CO_2$  conversions in plasma-assisted DRM reactions, especially at low temperatures. Such discrepancy was caused by the introduction of plasma which facilitated the direct  $CH_4$  dissociation [7,13,14,18,19]. The sluggish of  $CO_2$  activation rate in plasma-assisted DRM reaction indicates that design a catalyst with accelerated rate of  $CO_2$  activation is crucial to establish a matched rates of  $CH_4$  and  $CO_2$  conversion and thereby to establish a stable catalytic cycle for DRM.

Herein, as inspired by the superior ability of  $\beta$ - $Mo_2C$  for  $CO_2$  activation due to its unique surface properties of being an electron donor [20,21], it was employed as an effective component to activate  $CO_2$  and collaborated with  $Ni/\gamma-Al_2O_3$  for the plasma-assisted DRM reaction. By constructing such a bifunctional catalyst to regulate the  $CH_4$  and  $CO_2$  activation rates, a  $Mo_2C$ - $Ni/Al_2O_3$  catalyst possessing super activity and stability for the DRM reaction was obtained. Addition of  $\beta$ - $Mo_2C$  facilitated the charge deposition on the catalyst and a higher local electric field was formed as evidenced by the higher discharge power over  $Mo_2C$ - $Ni/Al_2O_3$  than  $Ni/Al_2O_3$  by using the same input power. Most significantly,  $Ni$  NPs were found to re-disperse over the  $\beta$ - $Mo_2C$  surface due to the strong interaction between  $Ni$  and  $\beta$ - $Mo_2C$ , resulting in formation of new active interface of  $Ni$ - $Mo_2C$  with better  $Ni$  dispersion. Benefiting from both  $CO_2$  dissociation catalyzed by  $\beta$ - $Mo_2C$  to reduce the carbon deposition and the better  $Ni$  dispersion to active  $CH_4$ , the  $Mo_2C$ - $Ni/Al_2O_3$  catalyst exhibited much better activity and improved stability as compared with the undoped  $Ni/Al_2O_3$  catalyst. The present study reveals the crucial roles of  $\beta$ - $Mo_2C$  additives in the plasma-assisted catalysis of DRM reaction in terms of affecting the discharge mode, re-dispersing of  $Ni$  NPs and facilitating the  $CO_2$  activation, providing practical solutions to improve the activity, stability as well as energy efficiency in coupled plasma and catalysis DRM reaction.

## 2. Experimental section

### 2.1. Catalyst preparation

The  $NiO/\gamma-Al_2O_3$  catalyst was prepared via incipient wetness impregnation (IWI) method. In detail,  $\gamma-Al_2O_3$  support was incipiently impregnated with an aqueous solution of  $Ni(NO_3)_2 \cdot 6H_2O$  (Sinopharm Chemical Reagent Co., Ltd) and then aged at room temperature for 24 h. After drying at  $110^\circ C$  overnight in oven, the impregnated precursor was calcined at  $500^\circ C$  for 4 h. The acquired catalyst was denoted as  $NiO/Al$ .

The  $\beta$ - $Mo_2C$  sample was prepared using a two-step temperature-programmed processes [22,23]:  $MoO_3$  particles were loaded in a quartz tube and carbonized in 20 vol%  $CH_4/H_2$  mixture (150 mL/min), firstly, the temperature was increased from room temperature to  $300^\circ C$  with a heating rate of  $5^\circ C/min$ , subsequently from  $300^\circ C$  ramped to  $700^\circ C$  with a heating rate of  $1^\circ C/min$ , and kept at  $700^\circ C$  for 2 h. After cooling down to ambient temperature, the obtained sample was passivated by exposing to 1 vol%  $O_2/Ar$  (30 mL/min) for 12 h.

$Mo_2C$ - $NiO/Al_2O_3$  catalysts with different  $Ni/Mo$  molar ratios (2/1, 1/2, 1/5) were prepared via a mechanical mixing method. Briefly, a certain amount of  $\beta$ - $Mo_2C$  sample was deeply physically mixed with  $NiO/Al_2O_3$  powder in an agate mortar for 60 min. The mixed catalysts details are listed in Table S1, and the synthesized samples are expressed as  $Mo_2C$ - $NiO/Al$ -x, where x represents the  $Ni/Mo$  molar ratio, namely 2, 1/2, 1/5.

Before reaction, the  $Mo_2C$ - $NiO/Al_2O_3$ -x catalyst was pretreated in 15 vol%  $CH_4/H_2$  mixture at  $500^\circ C$  for 1 h, and the  $NiO/Al_2O_3$  catalyst was pretreated in  $H_2$  at  $500^\circ C$  for 1 h, which was denoted as  $Mo_2C$ - $Ni/Al$ -x and  $Ni/Al$ , respectively.

### 2.2. Catalyst characterization

X-ray diffraction (XRD) patterns of the catalysts were obtained on an XRD-6000 (Shimadzu, Kyoto, Japan) with  $Cu K\alpha$  radiation source ( $\lambda = 0.1542$  nm), and operated at 30 kV and 30 mA. The step-scans were taken over  $2\theta$  range of  $20$ – $80^\circ$  at a scanning rate of  $10^\circ/min$ . Crystallographic information was obtained comparing XRD patterns to the Joint Committee on Powder Diffraction Standards (JCPDS).

BET surface area analysis of the catalysts was measured at  $-196^\circ C$  of liquid  $N_2$  temperature with an Autosorb-IQ-C sorption analyzer via Brunauer-Emmet-Teller (BJH) method.

The actual  $Ni$  and  $Mo$  contents of as-prepared catalysts were determined by inductively coupled plasma optical emission spectrometry (ICP-OES) on ICP-Optical Emission spectrometer (Model 2000, PerkinElmer).

X-ray photoelectron spectroscopy (XPS) experiments were performed on a spectrometer (ESCALAB 250XI, Thermo VG, America) using  $Al K\alpha$  source (1486.6 eV) run at 15 kV and 10 mA. The binding energy values of  $Ni$  and  $Mo$  species were corrected by the  $C 1s$  peak centered at 284.6 eV.

Transmission Electron Microscope (TEM) images of the catalysts were recorded on a Tecnai G2 F30 S-Twin system (Thermo Scientific, America) operated at the acceleration voltage of 300 keV. The sample was dispersed in absolute ethanol for 30 min under ultra-sonication condition and then dropped on a copper grid prior to measurement.

Carbon dioxide temperature-programmed surface reaction ( $CO_2$ -TPSR) was performed by a mass spectrometer (Omnistar™ Pfeiffer Vacuum, Germany). Typically, the catalysts were pretreated at  $500^\circ C$  for 1 h in  $H_2$  (or  $CH_4/H_2$ ) flow and then cooled down to  $50^\circ C$ . The 10 vol%  $CO_2/Ar$  with a total flow of 100 mL/min was fed to the reactor before the catalysts were heated from  $50^\circ C$  to  $900^\circ C$  and kept at  $900^\circ C$  for 10 min. The signal intensities of  $CO_2$  ( $m/z = 44$ ) and  $CO$  ( $m/z = 28$ ) were recorded.

Oxygen temperature-programmed oxidation ( $O_2$ -TPO) tests were performed using an infrared absorption spectrometer (SICK-MAIHAK-S710, Germany). The spent catalysts (0.025 g) were heated from  $50^\circ C$  to  $800^\circ C$  in flowing 5 vol%  $O_2/Ar$  at a linear heating rate of  $10^\circ C/min$ . The concentrations of  $CO_2$  and  $CO$  were directly measured online in the oxidation process.

Raman spectroscopy analysis was performed using DXR Microscope (Thermo Fisher, the United States) equipped with a 532 nm laser excitation. The Raman spectra were acquired in the range of  $1000$ – $3500$   $cm^{-1}$  and a resolution of  $2$   $cm^{-1}$  to verify the coke deposition styles of the spent catalysts.

### 2.3. Catalytic performance evaluations

#### 2.3.1. Experimental setup

The schematic diagram of plasma-assisted reforming system is shown in Fig. 1. The experiments were performed in a fixed-bed DBD reactor [22]. In brief, a quartz tube with a wall thickness of 1 mm and an outer diameter of 16 mm was served as dielectric layer. A grounded stainless-steel mesh was used as the outer electrode, which wrapped around the external surface of quartz tube. A stainless-steel rod with a diameter of 9 mm fixed at the axis of tube, which was acted as the inner electrode to connect with a high voltage AC power supply. The discharge length of this system was 10 mm, and the discharge gap between the two electrodes was 2.5 mm. A high voltage probe connected to the inner electrode measured the applied voltage in discharge process. The outer electrode was connected to an external capacitor ( $C_{ext} = 3.3$  nF) aiming to measure the total charge transferred in the discharge process. Both electrical signals produced on electrodes were recorded via a digital oscilloscope (Tektronix, TBS 2000 SERIES). The discharge power of DBD plasma was measured by the area calculation of the Lissajous figure. The current signals were determined with a digital oscilloscope through a standard resistance (51.2  $\Omega$ ). A K-type thermocouple with quartz-sealed

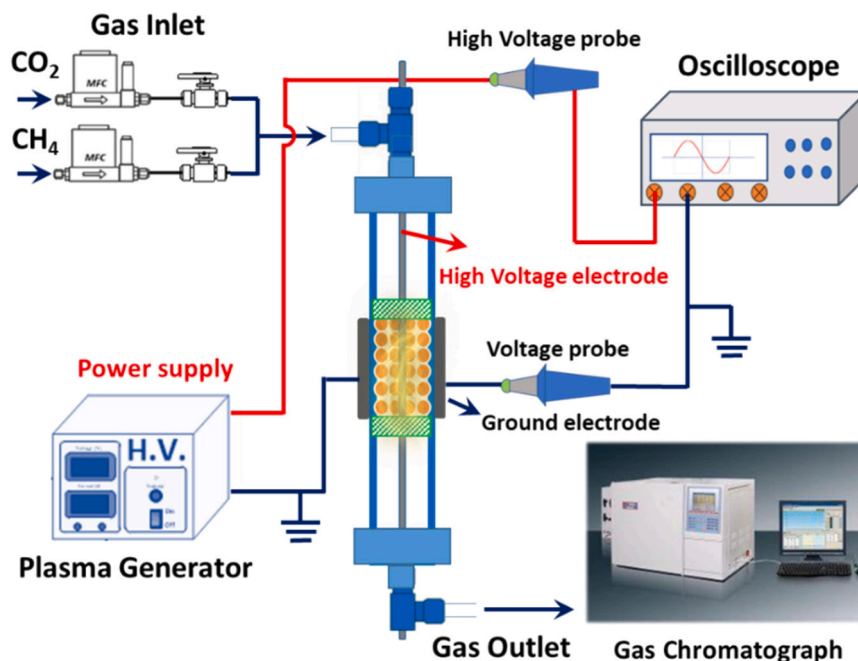


Fig. 1. Schematic diagram of the DBD plasma-catalytic reactor.

was fixed on outer electrode contacted with the catalytic bed to measure the variable temperatures of discharge zone in the reactor.

### 2.3.2. Pulse and stability performance tests in DBD-only without catalysts

Diluted CH<sub>4</sub> (1600 ppm CH<sub>4</sub> in Ar atmosphere) was fed into pure DBD plasma reactor (inner diameter of 8 mm, outer diameter of 10 mm) at different input powers (24 W, 34 W, 46 W) without any extra-thermal input. In the discharge process, the real-time concentration of CH<sub>4</sub> in the products was monitored and recorded simultaneously using an infrared absorption spectrometer (SICK-MAIHAK-S710, Germany). Similarly, dilute CO<sub>2</sub> (1900 ppm CO<sub>2</sub> in Ar atmosphere) was flowed into the reactor with DBD discharge, and the concentration of CO<sub>2</sub> in the products was measured online using the same spectrometer.

Stability test was performed under DBD-only condition. 0.20 g quartz sands were packed into the reactor, and then flowed a CH<sub>4</sub>/CO<sub>2</sub>/Ar mixing feed gas (volume ratio of 1/1/2, total flow rate of 62 mL/min). Then, the input power was adjusted to 45 W and generated plasma in discharge gap. Products were analyzed using a gas chromatograph (Model GC 7900, Tianmei, China) equipped with a thermal conductivity detector (TCD) and flame ionization detector (FID).

### 2.3.3. Plasma-catalytic performance evaluation

The plasma-catalytic DRM under different input powers (58.0 W, 74.0 W, 87.0 W, 107 W, 124 W, 132 W) without any extra-thermal input was performed in the fixed-bed reactor (inner diameter of 14 mm, outer diameter of 16 mm). 0.12 g Mo<sub>2</sub>C-NiO/Al-2 catalyst with 0.78 g of quartz sands was packed in the reactor. The Mo<sub>2</sub>C-NiO/Al-2 catalyst was pretreated in 15 vol% CH<sub>4</sub>/H<sub>2</sub> mixture (100 mL/min) at 500 °C for 1 h. After the temperature cooled down to room temperature, a flow of CH<sub>4</sub>/CO<sub>2</sub>/Ar (volume ratio: 1/1/8, 100 mL/min) was introduced into the reactor, corresponding to a weight hourly space velocity (WHSV) of 50,000 mL/g/h, and then increased the input power to generate the plasma in discharge gap without any extra-thermal input. In this test, the effluent gases from the outlet were analyzed by an online gas chromatograph (Model GC 7900, Tianmei, China) equipped with thermal conductivity detector (TCD) and flame ionization detector (FID).

In order to determine the optimal Ni/Mo molar ratio, the activity tests were performed over several Mo<sub>2</sub>C-NiO/Al catalysts in DRM under

plasma-catalysis condition. 0.12 g of catalyst mixed with quartz sands was loaded into the reactor, and then activated at 500 °C for 1 h under a 15 vol% CH<sub>4</sub>/H<sub>2</sub> stream (100 mL/min). After cooling down to room temperature, the feed gas (CH<sub>4</sub>/CO<sub>2</sub>/Ar with 1/1/8 ratio, 100 mL/min) was introduced at a WHSV of 50,000 mL/g/h, and the input power was performed at ca. 126 W. The effluent gases were measured online with the gas chromatograph.

The stability performances of different catalysts were evaluated by the fixed bed reactor in the plasma-assisted DRM reaction. In a typical procedure, 0.12 g of catalyst (40–60 mesh) mixed with 0.78 g of quartz sands (40–60 mesh) was placed between quartz wool plugs to form a 10 mm high catalyst bed in the tube. Prior to the experiment, the Mo<sub>2</sub>C-NiO/Al catalyst was pretreated in 15 vol% CH<sub>4</sub>/H<sub>2</sub> mixture (100 mL/min) at 500 °C for 1 h, while NiO/Al catalyst was pretreated in H<sub>2</sub> flow (100 mL/min) at 500 °C for 1 h. Following the pretreatment and then cooling down to room temperature, the catalysts were purged with a flow of CH<sub>4</sub>/CO<sub>2</sub>/Ar (volume ratio: 1/1/8, 100 mL/min), corresponding to a WHSV of 50,000 mL/g/h, and the input voltage was increased up to ca. 112 W. In this test, the conversion data were collected under steady-state condition. The blank experiment was conducted with fully packing quartz sands to explore the effect of quartz sands. 0.90 g quartz sands were pretreated in Ar at 400 °C for 0.5 h and other reaction conditions were the same as that of catalysts. The effluent gases were measured online with the gas chromatograph.

Conversions of CH<sub>4</sub> and CO<sub>2</sub>, selectivity of products (CO, C<sub>2</sub>, C<sub>3</sub>, H<sub>2</sub>), H<sub>2</sub>/CO ratio, carbon balance, discharge power (W) and energy efficiency (mmol/kJ) in the plasma-assisted DRM calculated according to the following equations:

$$X_{\text{CH}_4}(\%) = \frac{F_{\text{CH}_4,\text{in}} - F_{\text{CH}_4,\text{out}}}{F_{\text{CH}_4,\text{in}}} \times 100\% \quad (2)$$

$$X_{\text{CO}_2}(\%) = \frac{F_{\text{CO}_2,\text{in}} - F_{\text{CO}_2,\text{out}}}{F_{\text{CO}_2,\text{in}}} \times 100\% \quad (3)$$

$$S_{\text{CO}}(\%) = \frac{F_{\text{CO},\text{out}}}{(F_{\text{CH}_4,\text{in}} - F_{\text{CH}_4,\text{out}}) + (F_{\text{CO}_2,\text{in}} - F_{\text{CO}_2,\text{out}})} \times 100\% \quad (4)$$

$$S_{\text{C}_2}(\%) = \frac{2(F_{\text{C}_2\text{H}_4,\text{out}} + F_{\text{C}_2\text{H}_6,\text{out}})}{(F_{\text{CH}_4,\text{in}} - F_{\text{CH}_4,\text{out}}) + (F_{\text{CO}_2,\text{in}} - F_{\text{CO}_2,\text{out}})} \times 100\% \quad (5)$$

$$S_{C_3}(\%) = \frac{3(F_{C_3H_6,out} + F_{C_3H_8,out})}{(F_{CH_4,in} - F_{CH_4,out}) + (F_{CO_2,in} - F_{CO_2,out})} \times 100\% \quad (6)$$

$$S_{H_2}(\%) = \frac{F_{H_2,out}}{2(F_{CH_4,in} - F_{CH_4,out})} \times 100\% \quad (7)$$

$$H_2/CO = \frac{F_{H_2,out}}{F_{CO,out}} \times 100\% \quad (8)$$

$$C_{balance}(\%) = \frac{F_{CO,out} + 2(F_{C_2H_4,out} + F_{C_2H_6,out}) + 3(F_{C_3H_6,out} + F_{C_3H_8,out})}{(F_{CH_4,in} - F_{CH_4,out}) + (F_{CO_2,in} - F_{CO_2,out})} \times 100\% \quad (9)$$

$$P_{discharge} = f \int_0^T u dQ \quad (10)$$

$$E = \frac{n_{CH_4,converted} + n_{CO_2,converted}}{P_{discharge}} \quad (11)$$

$F_{in}$  and  $F_{out}$  refer to the reaction gas flow rate of inlet and outlet, respectively;  $f$  refers to frequency of discharge;  $Q$  refers to charge of discharge;  $u$  refers to the applied voltage;  $n_{CH_4,converted}$  and  $n_{CO_2,converted}$  refer to moles of converted  $CH_4$  and  $CO_2$ , respectively.

## 3. Results and discussion

### 3.1. Characterization of the catalysts

Fig. 2A showed the XRD patterns of the pre-reduced  $\beta$ - $Mo_2C$ , Ni/Al and  $Mo_2C$ -Ni/Al-2 samples. The diffraction peaks of Ni/Al catalyst consisted of  $Al_2O_3$  (JCPDS No. 75–0921),  $Ni^0$  (JCPDS No. 04–0850) and  $NiAl_2O_4$  (JCPDS No. 10–0339) phases. For the reduced  $Mo_2C$ -Ni/Al-2 catalyst, there were diffractions due to  $\beta$ - $Mo_2C$  (JCPDS No. 65–8766) and  $Al_2O_3$  (JCPDS No. 75–0921) observed. The diffractions of Ni species ( $Ni^0$  and  $NiAl_2O_4$ ) were difficult to detect due to the overlapped peaks of Ni,  $\beta$ - $Mo_2C$  and  $NiAl_2O_4$  species at ca.  $37$ – $44^\circ$ . It is noteworthy that there was an obvious diffraction peak ( $2\theta = 43.29^\circ$ ) of NiO phase (JCPDS No. 65–6920) over the untreated  $Mo_2C$ -NiO/Al-2 catalyst (Fig. 2B). Table 1 showed the BET surface areas and contents of Ni and Mo over Ni/Al and  $Mo_2C$ -Ni/Al-2 catalysts. The Ni/Al and  $Mo_2C$ -Ni/Al-2 catalysts had similar specific surface area, both higher than  $170 \text{ m}^2/\text{g}$  ( $\gamma$ - $Al_2O_3$  support had surface area of  $258 \text{ m}^2/\text{g}$ ). The Ni loadings of Ni/Al and  $Mo_2C$ -Ni/Al-2 catalysts were 6.8% and 6.6%, respectively.

TEM images of the reduced  $Mo_2C$ -Ni/Al-2 and Ni/Al catalysts were displayed in Fig. 3. As shown in Fig. 3A–B, the Ni/Al catalyst had a rod-like structure and distinct Ni aggregated particles were observed with an

**Table 1**

Textural properties and compositions of the reduced Ni/Al and  $Mo_2C$ -Ni/Al-2 catalysts.

Catalysts	$S_{BET}$ ( $\text{m}^2/\text{g}$ ) <sup>a</sup>	Ni size (nm) <sup>b</sup>	Compositions (wt%) <sup>c</sup>	
			Ni	Mo
$\gamma$ - $Al_2O_3$	258	–	–	–
Ni/Al	171	8.2	6.8	–
$Mo_2C$ -Ni/Al-2	185	5.3	6.6	5.8

<sup>a</sup> Surface area was determined from  $N_2$  adsorption-desorption isotherms;

<sup>b</sup> Mean size of Ni particles was measured by TEM images;

<sup>c</sup> The content of Ni and Mo was measured by ICP-AES results.

average size of ca. 8.2 nm. In comparison, the rod-like morphology belonging to  $\gamma$ - $Al_2O_3$  support was not clearly shown over  $Mo_2C$ -Ni/Al-2 catalyst (Fig. 3C), indicating that  $\gamma$ - $Al_2O_3$  surface might be covered by the mixed  $\beta$ - $Mo_2C$ . While some dark and round Ni particles can be still detected, being well dispersed with an average particle size of ca. 5.3 nm. STEM-EDX of the selected area confirmed that Ni and Mo species homogeneously distributed on the catalyst (Fig. 3F and G), and the Mo element was observed from the EDX analysis coexisted with Ni (Fig. 3I). Based on the above results and previous understanding on the strong interaction of additive metal with  $\alpha$ - $MoC$  substrate [23,24], it is suggested that the Ni- $Mo_2C$  interface was formed during the pretreatment and a re-dispersion of Ni induced by the strong interaction with  $\beta$ - $Mo_2C$  occurred over this mechanically mixed  $Mo_2C$ -Ni/Al-2 catalyst with a better Ni dispersion being achieved [25].

XPS analysis further confirmed the strong interaction between Ni and  $\beta$ - $Mo_2C$ , and the results were shown in Fig. 4. For the reduced Ni/Al catalyst, the Ni 2p spectra can be deconvoluted into three pairs, corresponding to the typical binding energies of three Ni species:  $Ni^0$  (Ni 2p<sub>3/2</sub> peak centered at 852.6 eV),  $Ni^{2+}$  of NiO in octahedral coordination sites (Ni 2p<sub>3/2</sub> peak centered at 855.4 eV) and  $NiAl_2O_4$  phase in tetrahedral coordination sites (Ni 2p<sub>3/2</sub> peak centered at 856.3 eV), respectively [26,27]. It is worthy to note that  $NiAl_2O_4$  species accounts for a larger proportion in Ni/Al catalyst, ca. 47% (Table 2). By comparison, in the case of the reduced  $Mo_2C$ -Ni/Al-2 catalyst, the prevalent Ni species are  $Ni_3C$  (Ni 2p<sub>3/2</sub> peak centered at 855.0 eV) [28] and the ratio of  $NiAl_2O_4$  decreases to 20%, indicating that the addition of  $\beta$ - $Mo_2C$  into Ni/Al sample enhances the interaction between  $\beta$ - $Mo_2C$  and Ni, and weakens the interaction between Ni with  $Al_2O_3$ , which inhibits the formation of  $NiAl_2O_4$  spinel [26].

Correspondingly, the Mo 3d spectrum of the reduced  $Mo_2C$ -Ni/Al-2 catalyst suggested that there are four different forms of Mo species on the catalyst, including  $Mo_2C$  (Mo 3d<sub>5/2</sub> peak centered at 228.1 eV), and Mo oxides identified as  $Mo^{4+}$  (Mo 3d<sub>5/2</sub> of 228.7 eV),  $Mo^{5+}$  (Mo 3d<sub>5/2</sub> of 231.1 eV),  $Mo^{6+}$  (Mo 3d<sub>5/2</sub> of 232.4 eV) [29]. The existence of  $MoO_x$  may be attributed to the surface oxidation during XPS sample transfer.

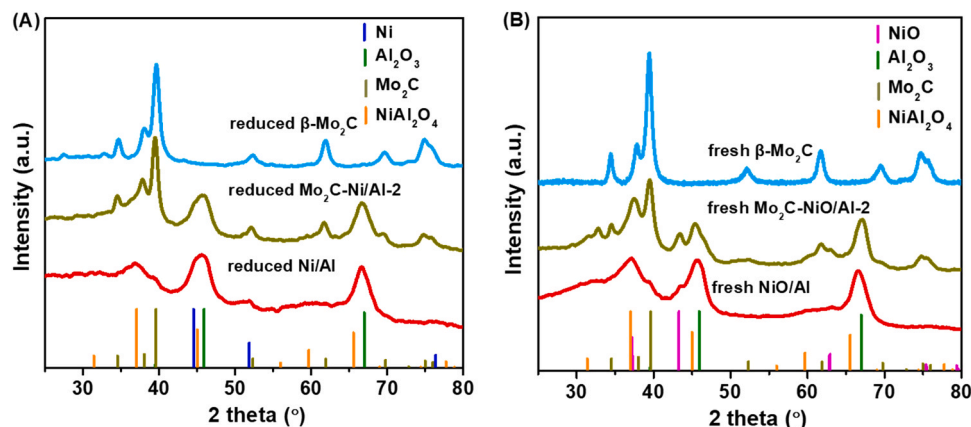


**Fig. 2.** (A) XRD patterns of reduced  $\beta$ - $Mo_2C$ , Ni/Al and  $Mo_2C$ -Ni/Al-2 catalysts; (B) XRD patterns of fresh  $\beta$ - $Mo_2C$ , NiO/Al and  $Mo_2C$ -NiO/Al-2 catalysts.



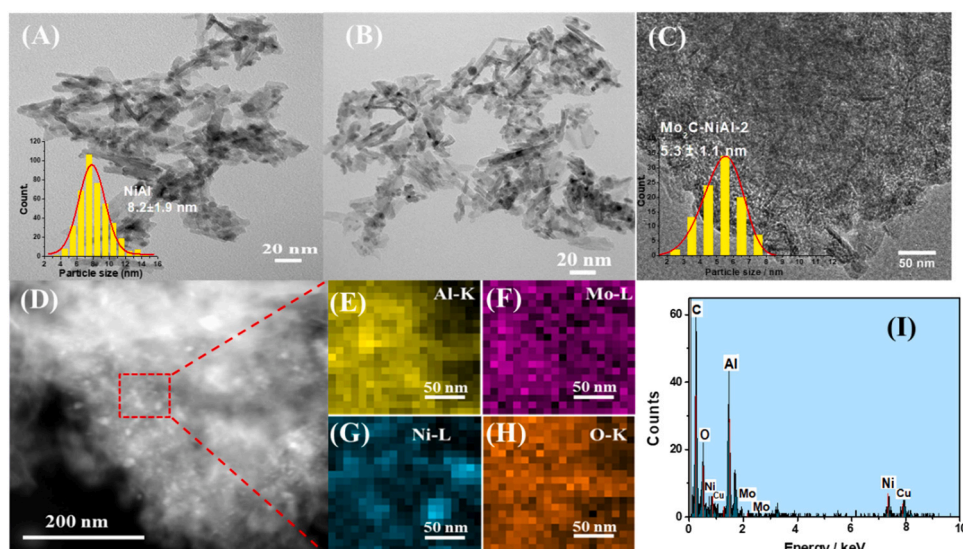


**Fig. 3.** Electron microscopy images of the reduced catalysts. (A–B) TEM images of the reduced Ni/Al catalyst; (C) TEM image of the reduced Mo<sub>2</sub>C-Ni/Al-2 catalyst; (D) STEM image of the reduced Mo<sub>2</sub>C-Ni/Al-2 catalyst and (E–H) the corresponding mapping with (I) EDX spectrum of the selected area marked in red box in (D). The Ni particle size distribution for Ni/Al and Mo<sub>2</sub>C-Ni/Al-2 catalysts are inserted in (A) and (C), respectively.

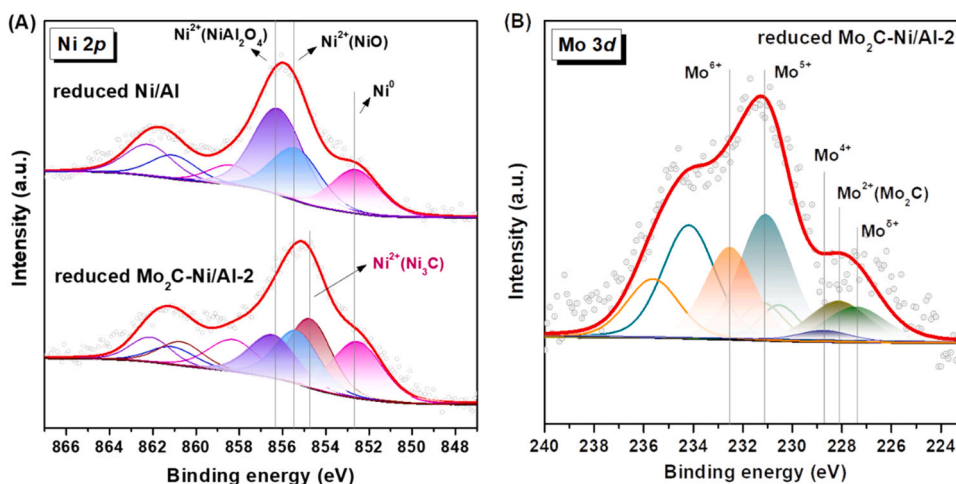


**Fig. 4.** (A) Ni 2p XPS spectra of the reduced Ni/Al and Mo<sub>2</sub>C-Ni/Al-2 catalysts (The catalysts were activated by the gas of H<sub>2</sub> and CH<sub>4</sub>/H<sub>2</sub> (15/85) at 500 °C for 1 h, respectively); (B) Mo 3d XPS spectrum of the reduced Mo<sub>2</sub>C-Ni/Al-2 catalyst (The catalysts were activated by the gas of CH<sub>4</sub>/H<sub>2</sub> (15/85) at 500 °C for 1 h).

**Table 2**

XPS-derived characteristics of Ni 2p and Mo 3d spectra over the reduced Ni/Al and Mo<sub>2</sub>C-Ni/Al-2 catalysts.

Catalysts	Ni 2p <sub>3/2</sub> (%)				Mo 3d <sub>5/2</sub> (%)				
	Ni <sup>0</sup>	Ni <sup>+</sup> (Ni <sub>3</sub> C)	Ni <sup>2+</sup> (NiO)	Ni <sup>2+</sup> (NiAl <sub>2</sub> O <sub>4</sub> )	Mo <sup>δ+</sup> (0 < δ < 2)	Mo <sup>2+</sup> (Mo <sub>2</sub> C)	Mo <sup>4+</sup>	Mo <sup>5+</sup>	Mo <sup>6+</sup>
Ni/Al	23.5	–	28.7	47.9	–	–	–	–	–
Mo <sub>2</sub> C-Ni/Al-2	27.8	28.9	23.2	20.1	13.0	14.6	3.30	40.7	28.4

There are Mo<sup>δ+</sup> species (0 < δ < 2, Mo 3d<sub>5/2</sub> of 227.5 eV) emerged besides β-Mo<sub>2</sub>C (228.1 eV). The above results indicate that after mixing with β-Mo<sub>2</sub>C, Ni interacts with β-Mo<sub>2</sub>C to form Ni<sub>3</sub>C motifs (corresponding to the Ni 2p<sub>3/2</sub> peak centered at 855.0 eV), which reduces the coordination between Mo and C, thereby declines the valence of Mo in β-Mo<sub>2</sub>C to lower value of 0 < δ < 2. The similar results of Ni-C species between Ni and α-MoC were reported by Ma et al. [30]. Such a strong interaction leads to redispersion of Ni over β-Mo<sub>2</sub>C and generates active Ni-Mo<sub>2</sub>C interface for DRM reaction.

CO<sub>2</sub>-TPSR was employed here to study the activation of CO<sub>2</sub> over Mo<sub>2</sub>C-Ni/Al-2 catalyst, shown in Fig. 5. The consumption of CO<sub>2</sub> (m/

z = 44) started at 453 °C and simultaneously accompanied with CO (m/z = 28) formation (Fig. 5A), indicating that CO<sub>2</sub> could dissociate to generate CO even at 450 °C over Mo<sub>2</sub>C-Ni/Al-2 catalyst, which is consistent with our previous result that β-Mo<sub>2</sub>C facilitates CO<sub>2</sub> activation and dissociation at low temperatures [20]. For the reference Ni/Al catalyst (Fig. 5B), no CO<sub>2</sub> consumption and CO formation were observed in the whole temperature range, suggesting CO<sub>2</sub> can be not dissociated over Ni/Al catalyst.

The Lissajous figures during the DBD discharge with different packing materials were shown in Fig. 6 at a constant input power of ca. 112 W. When quartz sands, Ni/Al and Mo<sub>2</sub>C-Ni/Al-2 materials were

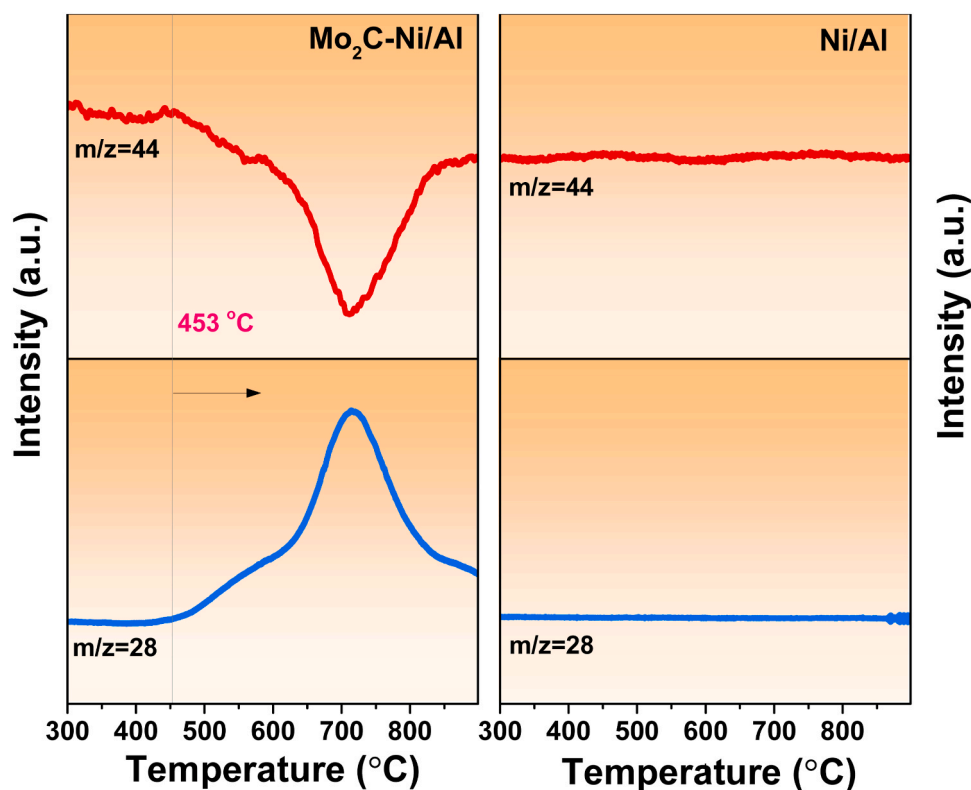


Fig. 5. CO<sub>2</sub>-TPSR profiles of the fresh Mo<sub>2</sub>C-Ni/Al-2 and Ni/Al catalysts with a heating rate of 10 °C/min from 50 °C to 900 °C in 10 vol% CO<sub>2</sub>/Ar flow (100 mL/min).

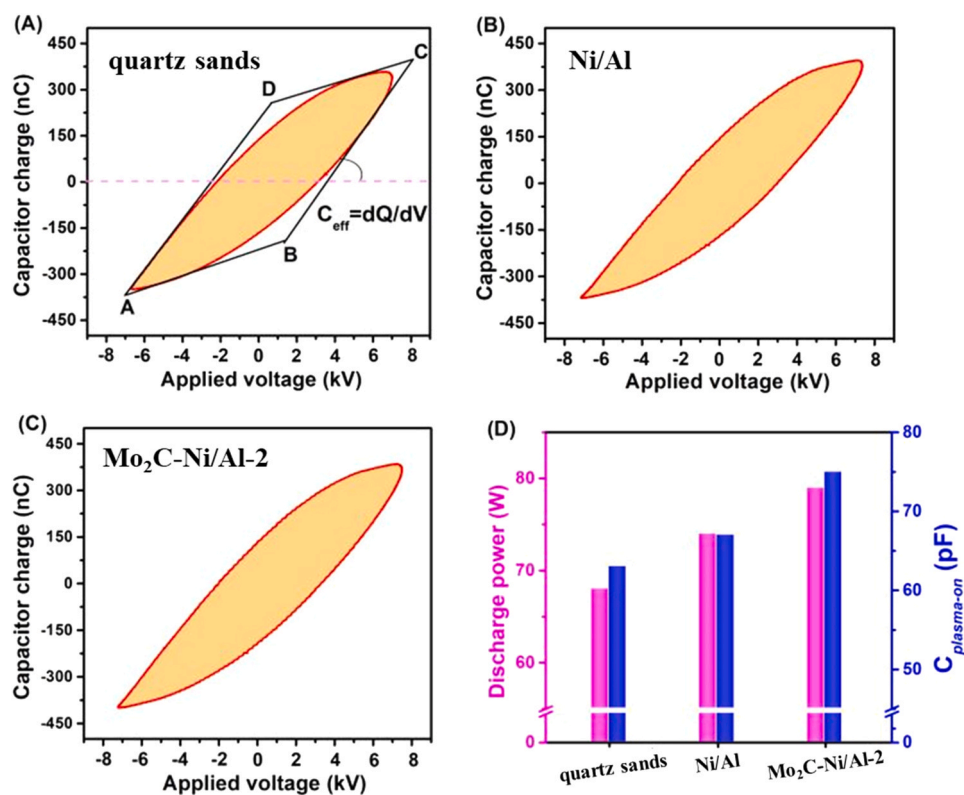


Fig. 6. Q-U Lissajous figures, discharge power and effective capacitance of quartz sands, Ni/Al and Mo<sub>2</sub>C-Ni/Al-2 in plasma-catalytic DRM reaction. Reaction conditions: discharge length = 10 mm, input power = 112 W, WHSV = 50,000 mL/g/h, CH<sub>4</sub>/CO<sub>2</sub>/Ar = 1/1/8, the temperature of catalytic bed was ca. 470 °C and there was no additional thermal input.

packed into the reactor, respectively, the shapes of Lissajous figures were almost the same, in form of oval, indicating that the predominant surface discharges occurred over all the materials. Furthermore, the effective capacitance of DBD (the slope of lines BC and AD in Fig. 6A) for the Mo<sub>2</sub>C-Ni/Al-2 catalyst (75 pF) was highest among the three packing materials (quartz sands of 63 pF and Ni/Al of 67 pF) (Table 3). As a result, the discharge powers calculated from the areas of Lissajous plot decreased in the following sequence: Mo<sub>2</sub>C-Ni/Al-2 (79 W) > Ni/Al (74 W) > quartz sands (68 W). Compared to the quartz sands, the catalysts with abundant metallic Ni species packed in the reactor were conductive, which contributed to the increase of discharge power [31]. Especially, in the case of the Mo<sub>2</sub>C-Ni/Al-2 catalyst, the discharge power was further increased, indicating that packing  $\beta$ -Mo<sub>2</sub>C material in the discharge region facilitated the charge accumulation, and thereby enhanced the discharge power [22]. Meanwhile, the density and amplitude of current filaments were stronger over Mo<sub>2</sub>C-Ni/Al-2 than that of Ni/Al, suggesting that more discharge channels were generated on Mo<sub>2</sub>C-Ni/Al-2 (Fig. S1).  $\beta$ -Mo<sub>2</sub>C being one of transition metal carbides has good electrical and thermal conductivity [32–34], contributing to the enhanced charge transferring density.

### 3.2. DBD-only towards CH<sub>4</sub> and CO<sub>2</sub> activation without catalysts

To study the activation of CH<sub>4</sub> and CO<sub>2</sub> under DBD-only conditions, diluted CH<sub>4</sub> (1600 ppm CH<sub>4</sub> in Ar) or diluted CO<sub>2</sub> (1900 ppm CO<sub>2</sub> in Ar) was fed individually into the reactor (packed with quartz sands without catalysts) operating at different input powers (24 W, 34 W, 46 W) without external heating. As shown in Fig. 7A, the conversions of CO<sub>2</sub> increased from 40% to 50% with increasing input power. Comparatively, CH<sub>4</sub> conversions were much higher, ranging from 84% to 93%. This indicates that CH<sub>4</sub> is easily dissociated by DBD plasma as compared with CO<sub>2</sub>, which should be related to the fact that the C-H bond dissociation energy (4.5 eV) of CH<sub>4</sub> is lower than the C=O bond dissociation energy (5.5 eV) of CO<sub>2</sub> [35]. Fig. 7B showed the conversions of CH<sub>4</sub> and CO<sub>2</sub> when they were co-fed (CH<sub>4</sub>/CO<sub>2</sub>/Ar = 1/1/2) under DBD-only condition. Compared to the conversion of CO<sub>2</sub>, the conversion of CH<sub>4</sub> was much higher, being consistent with the above results. It is worthy to note that the conversion of CH<sub>4</sub> rapidly decreased with time-on stream, and carbon deposition was detected on the inner surface of the quartz tube and inner electrode, indicating that the mismatch of CH<sub>4</sub> and CO<sub>2</sub> reaction rates led to the coke deposition when no catalyst was packed in DBD plasma. Accordingly, it is crucial to enhance CO<sub>2</sub> activation by catalysis to match the rates of CH<sub>4</sub> and CO<sub>2</sub> dissociation.

### 3.3. Effect of input power to adjust the balanced rates for CH<sub>4</sub> and CO<sub>2</sub> conversion

When DBD was coupled with Mo<sub>2</sub>C-Ni/Al-2 catalyst (the optimized Ni/Mo molar ratio of 2, Fig. S2), the effects of input power were investigated to tune the balanced conversion rates towards CH<sub>4</sub> and CO<sub>2</sub>, and the results were shown in Fig. 8. In Fig. 8A, it is clear to note that below 80 W, CH<sub>4</sub> and CO<sub>2</sub> conversions dropped with increasing input power; however, above 80 W, the conversions enhanced with rising the input power. Meanwhile, the discharge modes changed with increasing the input power as indicated by the Lissajous patterns

changing from a parallelogram shape below 80 W to an oval-like shape at higher input power, implicating an evolution from filamentary discharge to surface discharge and catalysis functioned above 80 W (Fig. 9). These results, in turn, help us to understand the opposite trends at 80 W being observed in Fig. 8A. The increased CH<sub>4</sub> and CO<sub>2</sub> conversions above 80 W, especially the conversion of CO<sub>2</sub> became even higher than that of CH<sub>4</sub> at 132 W, implied that the catalytic role of Mo<sub>2</sub>C-Ni/Al-2 catalyst was obviously improved, which contributed to the increased CO<sub>2</sub> conversion. This is remarkable that the balanced CH<sub>4</sub> and CO<sub>2</sub> conversion rates are crucial to keep a stable performance for DRM reaction. When the input power is below 80 W, it is mostly a filamentary discharge with seldom contributions from catalysis (Fig. 9), being consistent with the higher CH<sub>4</sub> conversion rate than CO<sub>2</sub> under DBD-only condition. This led to the carbon deposition over the catalyst, and thereby the decreased conversions at 74 W.

For carbon products, with increasing the input power, the selectivity of CO increased from 45% to 88%, and the selectivity of C<sub>2</sub> (mainly ethane) and C<sub>3</sub> (propane) decreased from 18.7% to 1.7% and from 7.6% to 0.7%, respectively (Fig. 8B). The carbon balance was gradually increased from 69% to 91% when increasing the input power from 58 W to 124 W (Fig. S3), suggesting more coke deposited on the catalyst at lower input power, which was consistent with the decrease of activity at the input power of 74 W (below 80 W). Higher than this, the synergy between plasma and catalysis became significant and therefore the CH<sub>4</sub> and CO<sub>2</sub> conversions enhanced again.

### 3.4. Comparison of Ni/Al and Mo<sub>2</sub>C-Ni/Al-2 catalysts for DBD-assisted DRM reaction

The catalytic performance of Ni/Al and Mo<sub>2</sub>C-Ni/Al-2 catalysts was compared at input power of 112 W (without extra heating input) to illuminate the role of  $\beta$ -Mo<sub>2</sub>C in plasma-assisted DRM reaction. As shown in Fig. 10, a blank experiment by packing quartz sands in the discharge zone was also performed. It showed quite low conversions (CH<sub>4</sub> conversion of ~15%, CO<sub>2</sub> conversion of ~6%). Comparatively, the plasma-catalytic system by packing Mo<sub>2</sub>C-Ni/Al-2 catalyst enhanced the initial conversions of CH<sub>4</sub> and CO<sub>2</sub> to above 80%. For Ni/Al catalyst, the catalytic activity rapidly declined, and the conversions of CH<sub>4</sub> and CO<sub>2</sub> decreased from 75.4% to 51.6% and from 74.2% to 53.6% within 675 min of time on stream, respectively (Fig. 10A-B). It is clearly noted that the initial conversions of CH<sub>4</sub> and CO<sub>2</sub> for Mo<sub>2</sub>C-Ni/Al-2 catalyst were higher (82.5% and 84.6%) compared with that of Ni/Al catalyst, and showed much stable performance within the tested hours. This suggests that the cooperation of  $\beta$ -Mo<sub>2</sub>C with Ni/Al catalyst can markedly improve the catalytic conversions as well as stability towards plasma-catalytic DRM reaction. The enhanced conversions should be related to the improved Ni dispersion after  $\beta$ -Mo<sub>2</sub>C mixing.

In addition to CO, C<sub>2</sub> and C<sub>3</sub> were also detected in the carbon products, including C<sub>2</sub>H<sub>4</sub>, C<sub>2</sub>H<sub>6</sub>, C<sub>3</sub>H<sub>6</sub>, C<sub>3</sub>H<sub>8</sub> (Fig. S4). For the quartz sands packing, the selectivity of CO, C<sub>2</sub> (C<sub>2</sub>H<sub>4</sub>, C<sub>2</sub>H<sub>6</sub>) and C<sub>3</sub> (C<sub>3</sub>H<sub>6</sub>, C<sub>3</sub>H<sub>8</sub>) was 40%, 16.1% and 6.5%, respectively, and C<sub>2</sub>H<sub>6</sub> was the dominant hydrocarbon product. The selectivity of CO over Ni/Al catalyst was obviously increased to 85%, whereas that of C<sub>2</sub> and C<sub>3</sub> was decreased to 2.5% and 0.9%, respectively, suggesting the selectivity of targeted products can be improved via combine DBD plasma with catalyst. The addition of  $\beta$ -Mo<sub>2</sub>C further increased the selectivity of CO (89.5%), and the selectivity of C<sub>2</sub> and C<sub>3</sub> decreased to below 2% (Fig. 10C) over Mo<sub>2</sub>C-Ni/Al-2 catalyst. Meanwhile, the selectivity of H<sub>2</sub> was 47.8% over quartz sands, 87.2% over Ni/Al catalyst and 92.7% over Mo<sub>2</sub>C-Ni/Al-2 catalyst, respectively (Fig. 10D). The increase of selectivity to H<sub>2</sub> was due to the suppression of C<sub>2</sub> and C<sub>3</sub> production over catalysts. The H<sub>2</sub>/CO ratio in syngas over Ni/Al and Mo<sub>2</sub>C-Ni/Al-2 catalysts was 1.07 and 1.03, respectively, which is an ideal feedstocks for the synthesis of oxygenates (e.g. acetic acid, dimethyl ether, oxoalcohols) [36]. Additionally, the carbon balance of Mo<sub>2</sub>C-Ni/Al-2 catalyst was higher than that of Ni/Al (Fig. S6), implying that the former has

**Table 3**

Summary of input powers, corresponding discharge powers and effective capacitances over three different packing materials in the plasma-assisted DRM reaction.

Packing materials	Input power (W)	Discharge power (W)	Effective capacitance (pF)
Quartz sands	112	68	63
Ni/Al	112	74	67
Mo <sub>2</sub> C-Ni/Al-2	112	79	75

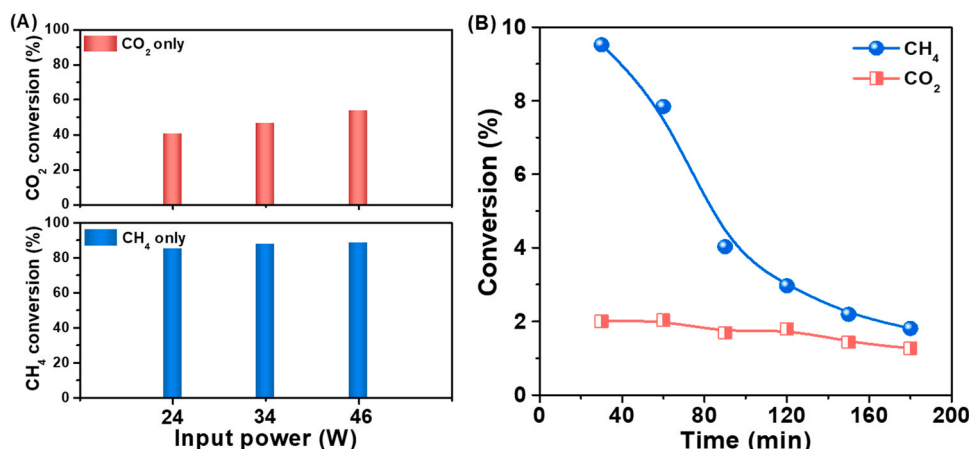


**Fig. 7.** (A) Conversions of CH<sub>4</sub>-only and CO<sub>2</sub>-only with different input powers under the pure DBD plasma condition without external heating (CH<sub>4</sub>-only condition: 1600 ppm CH<sub>4</sub>/Ar, F = 100 mL/min; CO<sub>2</sub>-only condition: 1900 ppm CO<sub>2</sub>/Ar, F = 100 mL/min). (B) Stability performance for DRM reaction under the pure DBD plasma condition (Reaction conditions: CH<sub>4</sub>/CO<sub>2</sub>/Ar = 1/1/2, input power = 45 W, F = 62 mL/min).

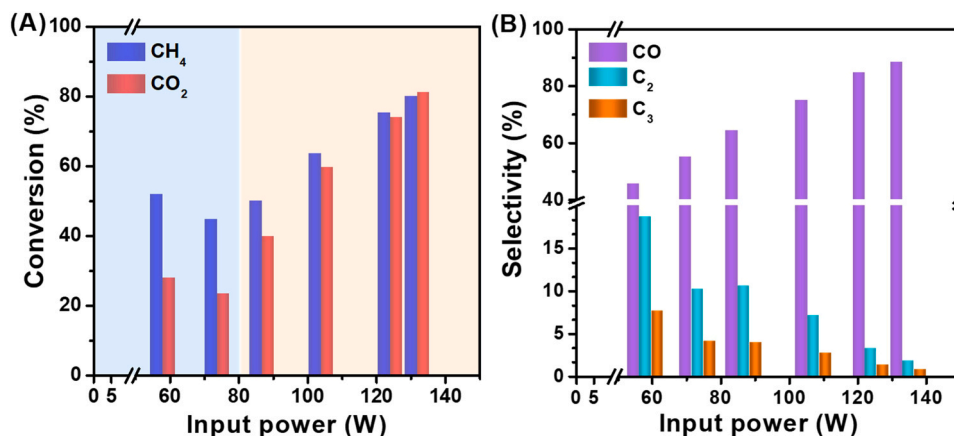


**Fig. 8.** (A) Catalytic performance and (B) carbon products distribution at different input powers over the Mo<sub>2</sub>C-Ni/Al-2 catalyst under plasma-catalysis condition. Reaction conditions: WHSV = 50,000 mL/g/h, discharge length = 10 mm, CH<sub>4</sub>/CO<sub>2</sub>/Ar = 1/1/8, the temperature of catalytic bed was ca.170–425 °C and there was no additional thermal input.

a better resistance of coke deposition during the plasma-catalytic DRM process.

Fig. 11 showed the influence of the catalysts on the energy efficiency of the plasma-assisted dry reforming of methane process under the kinetic region to exclude the external diffusion (Fig. S6). Clearly, compared to the plasma-only reaction, the plasma-catalytic coupling enhanced the energy efficiency due to the generation of the plasma-catalytic synergy effect. And in the plasma-catalytic DRM process, the use of Mo<sub>2</sub>C-promoted catalyst (0.64 mmol/kJ) showed higher energy efficiency compared to the reaction over the Ni/Al catalyst (0.25 mmol/kJ). Table S2 presents a summary of catalytic performances and energy efficiencies over different DBD systems for the plasma-assisted DRM reaction. The higher energy efficiency was achieved when placing the Mo<sub>2</sub>C-Ni/Al-2 catalyst in the plasma-catalytic reforming process.

### 3.5. Characterization of the spent catalysts

To understand the role of  $\beta$ -Mo<sub>2</sub>C in this plasma-catalysis coupling DRM reaction, the spent catalysts were characterized via XRD, TEM, O<sub>2</sub>-TPO and Raman spectra.

The XRD patterns of the spent catalysts were shown in Fig. 12. For the spent Ni/Al sample, the XRD patterns showed a sharp diffraction peak of graphite carbon ( $2\theta = 26.2^\circ$ , JCPDS No. 26-1080), indicating that there is serious carbon deposition during the reaction. While for the

spent Mo<sub>2</sub>C-Ni/Al-2 catalyst, the diffraction peak of the deposited carbon was quite weak, in accordance with its good catalytic stability in the DRM reaction. SEM images revealed that there were two types of carbon species deposited on the surface of the catalysts, including amorphous carbon and filamentous carbon (Fig. S7), which is in good accordance with XRD patterns of the carbon diffraction (Fig. 12).

O<sub>2</sub>-TPO experiments further supported the above conclusion, which was shown in Fig. 13A. It should be noted that only a trace amounts of CO were formed during the oxidation process (Fig. S8). The oxidation of deposited carbon generated overlapped CO<sub>2</sub> peaks ranging from 300 to 750 °C, being ascribed to the oxidation of amorphous carbon (ca. 500 °C), filamentous carbon (ca. 610–630 °C) and graphitic carbon (ca. above 650 °C) [37–39]. Obviously, the amount of filamentous carbon over spent Ni/Al catalyst was much more than that of spent Mo<sub>2</sub>C-Ni/Al-2 catalyst, which is consistent with XRD results (Fig. 12). It has been suggested that the filamentous carbon and graphitic carbon formed in the DRM reaction are inactive because of the relatively high oxidation temperature than amorphous one, which is the main reason of catalysts deactivation [38,40]. The quantitative analysis of coke deposition was shown in Fig. 13B. It is obvious that the total amount of carbon deposits was 8.8 mmol C/g<sub>cat</sub> over the spent Ni/Al catalyst, which is ca. twice of that over the spent Mo<sub>2</sub>C-Ni/Al-2 catalyst. It is worth noting that oxidation of  $\beta$ -Mo<sub>2</sub>C itself produced CO<sub>2</sub> as well, corresponding to 0.8 mmol C/g<sub>cat</sub>. Considering this contribution, the net amount of coke



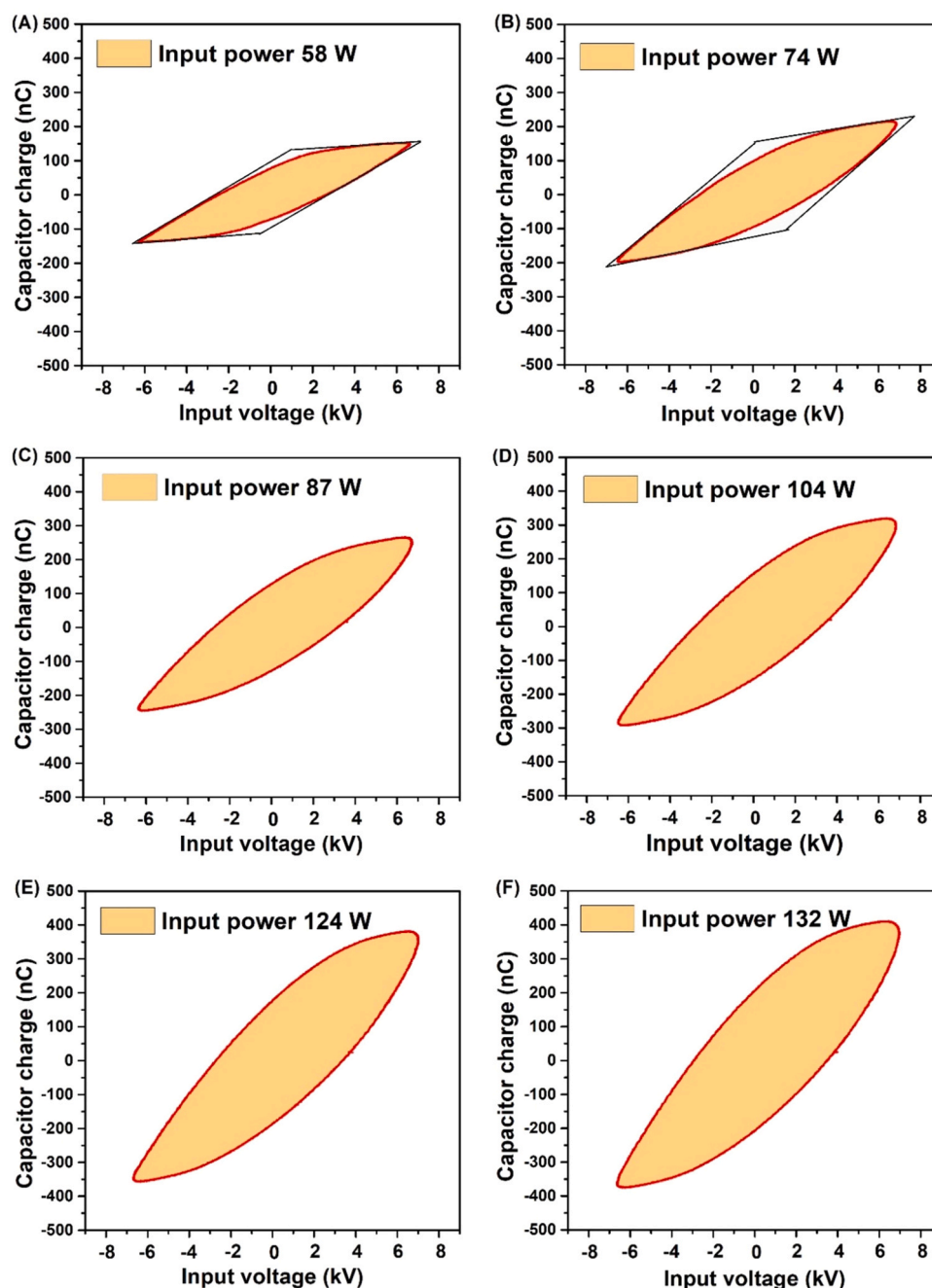


**Fig. 9.** Lissajous figures of the  $\text{Mo}_2\text{C-Ni/Al-2}$  catalyst at different input powers under the plasma-catalytic condition. Conditions: WHSV = 50,000 mL/g/h, discharge length = 10 mm,  $\text{CH}_4/\text{CO}_2/\text{Ar} = 1/1/8$ , the temperature of catalytic bed was ca.170–425 °C and there was no additional thermal input.

deposits was ca. 3 times less over the spent  $\text{Mo}_2\text{C-Ni/Al-2}$  catalyst than Ni/Al catalyst. Therefore, it can be illustrated that the addition of  $\beta\text{-Mo}_2\text{C}$  is able to obviously suppress the coke generation owing to enhance activation of  $\text{CO}_2$ , and improve the stability performance on plasma-assisted DRM.

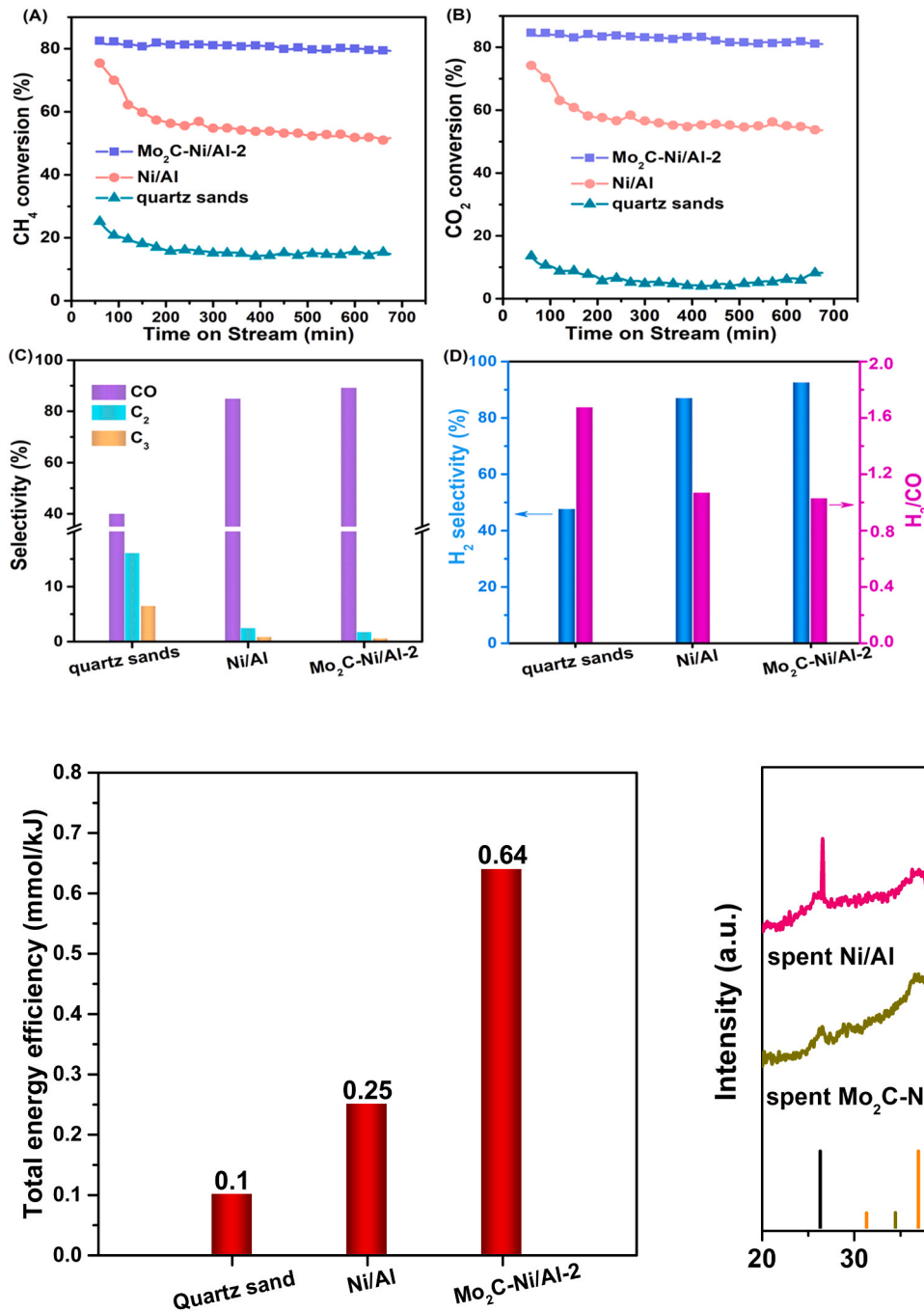
Raman spectra were performed to further study the structure of coke deposited on the spent catalysts (Fig. 13C). The relative intensity of G band (located at  $1578\text{ cm}^{-1}$  and was ascribed to the stretching mode of the  $\text{sp}^2$  bond in ordered graphite) and D band (located at  $1345\text{ cm}^{-1}$  and was assigned to disordered carbon species) represents the graphitization of coke deposits, and the degree of graphitization enhanced with increasing the  $I_G/I_D$  ratio [41,42]. For the reduced  $\text{Mo}_2\text{C-Ni/Al-2}$  catalyst, Raman signal was not detected between 1000 and  $3500\text{ cm}^{-1}$ . Fig. 13D showed that  $I_G/I_D$  ratio value for the spent Ni/Al catalyst (0.93)

was higher than that of the spent  $\text{Mo}_2\text{C-Ni/Al-2}$  catalyst (0.83), heralding the degree of carbon crystallinity on spent Ni/Al was higher compared with that on spent  $\text{Mo}_2\text{C-Ni/Al-2}$ , and the carbon deposited on Ni/Al required higher temperature to eliminate, which was well agreement with the results of the  $\text{O}_2\text{-TPO}$  experiments. In a word, the introduction of  $\beta\text{-Mo}_2\text{C}$  clearly decreased the crystallinity of deposited carbon formed and inhibited coke deposited on the catalysts, which was beneficial to improve the catalytic stability.

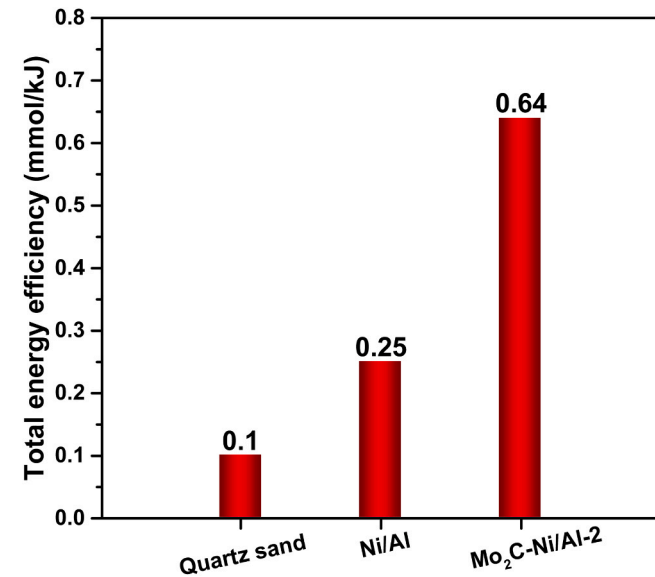
### 3.6. Discussion

#### 3.6.1. Plasma-only dry reforming of $\text{CH}_4$ with $\text{CO}_2$

Non-thermal plasma (NTP) provides a promising alternative to thermal catalytic approach for the activation and conversion of the

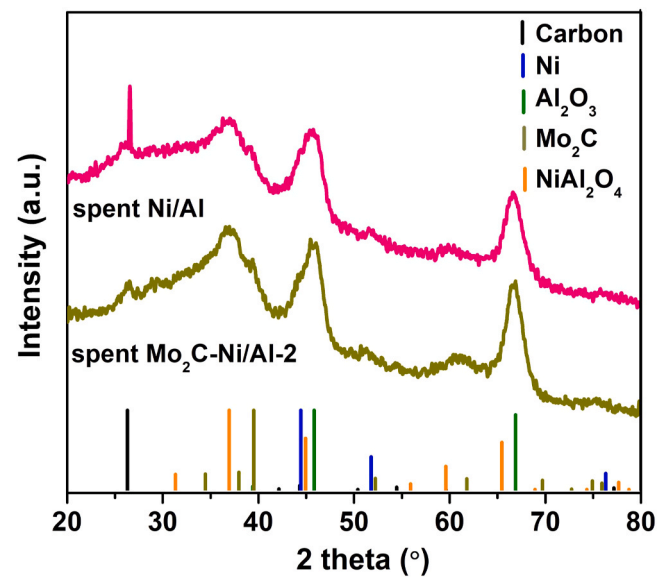


**Fig. 10.** Stability performance of the Mo<sub>2</sub>C-Ni/Al-2, Ni/Al and quartz sands (the blank experiment) in the DRM reaction under plasma-catalytic condition. (A) CH<sub>4</sub> conversion; (B) CO<sub>2</sub> conversion; (C) the selectivity of CO, C<sub>2</sub>, C<sub>3</sub> products from the gas analysis at reaction time of 675 min; (D) the selectivity of H<sub>2</sub> and H<sub>2</sub>/CO ratio from the gas analysis at reaction time of 675 min. Reaction conditions: discharge length = 10 mm, input power = 112 W, WHSV = 50,000 mL/g/h, CH<sub>4</sub>/CO<sub>2</sub>/Ar = 1/1/8, the temperature of catalytic bed was ca. 470 °C and there was no additional thermal input.

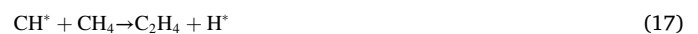


**Fig. 11.** Effect of different packing materials on the total energy efficiency for the plasma-catalytic DRM process, which were measured in the kinetic region. Reaction conditions: discharge length = 10 mm, input power = 112 W, WHSV = 1,750,000 mL/g/h, CH<sub>4</sub>/CO<sub>2</sub>/Ar = 3/3/2.

highly stable CH<sub>4</sub> and CO<sub>2</sub> molecules, which can generate numerous highly energetic electrons with a typical electron energy of 1–10 eV and maintain the overall gas temperature as low as room temperature. Recent simulation of plasma CH<sub>4</sub> conversion has shown that the electron-impact dissociation of CH<sub>4</sub> leads to 79% CH<sub>3</sub>, 15% CH<sub>2</sub> and 5% CH radical formation, respectively [43,44]. In addition, experimental results revealed that direct CH<sub>4</sub> decomposition by electrons could also occur to generate H<sub>2</sub> and solid carbon [45]. And free recombination of reactive species formed by gas-phase electron impact results in the poor selectivity of carbon products, and the possible elementary reactions are listed as Eqs. (12)–(20) [13,46,47].



**Fig. 12.** XRD patterns of the spent Ni/Al and Mo<sub>2</sub>C-Ni/Al-2 catalysts after stability tests for 675 min (Reaction conditions: WHSV = 50,000 mL/g/h, input power = 112 W).



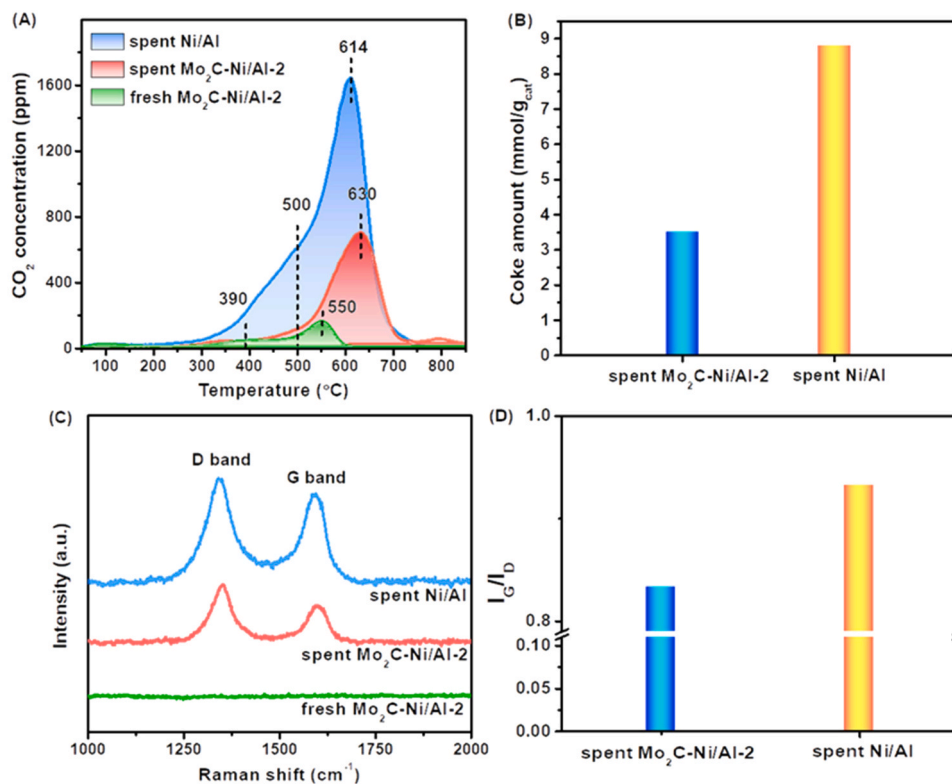
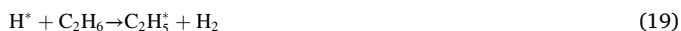


**Fig. 13.** (A) O<sub>2</sub>-TPO profiles of the fresh Mo<sub>2</sub>C-Ni/Al-2, spent Mo<sub>2</sub>C-Ni/Al-2 and spent Ni/Al catalysts; (B) Amount of coke over the spent catalysts from the O<sub>2</sub>-TPO analysis; (C) Raman spectra of the spent Ni/Al and Mo<sub>2</sub>C-Ni/Al-2 catalysts; (D) I<sub>G</sub>/I<sub>D</sub> ratio of the spent catalysts after stability tests. (Reaction conditions: WHSV = 50,000 mL/g/h, input power = 112 W, time on stream: 675 min).



The symbol “\*” represents the excited state.

This is in line with the experimental results shown in Fig. 10 (C), where there is a wide distribution of carbon products. The selectivity of CO, C<sub>2</sub> (C<sub>2</sub>H<sub>4</sub>, C<sub>2</sub>H<sub>6</sub>) and C<sub>3</sub> (C<sub>3</sub>H<sub>6</sub>, C<sub>3</sub>H<sub>8</sub>) in the effluent gas was 40%, 16.1% and 6.5%, respectively, and a low carbon balance of 65% was obtained.

For CO<sub>2</sub> conversion, CO<sub>2</sub> dissociation by electron impact vibrational excitation is the most effective pathway in non-thermal plasma and that up to 97% of the plasma energy can be transferred from electrons to vibrational excitation of CO<sub>2</sub> [48]. The electron impact dissociation of vibrationally excited CO<sub>2</sub> species was the most significant channel to generate CO product in the gas-phase (Eqs. (21) and (22)) [49].



Owing to the fact that C-H bond dissociation energy (4.5 eV) of CH<sub>4</sub> is lower than C=O bond dissociation energy (5.5 eV) of CO<sub>2</sub>, and the cross sections of CH<sub>4</sub> for electron impact excitation is higher than that of CO<sub>2</sub> at 10–1000 eV [50,51], it is reasonable to believe that more reaction channels exist for CH<sub>4</sub> conversion as compared to CO<sub>2</sub> dissociation under plasma-only conditions. This has been clearly shown in Fig. 7, where CH<sub>4</sub> conversions are greater than CO<sub>2</sub> conversions at various input powers. And the mismatch of CH<sub>4</sub> and CO<sub>2</sub> conversion rates easily leads to carbon deposition and rapid deactivation.

### 3.6.2. Plasma-catalytic dry reforming of CH<sub>4</sub> with CO<sub>2</sub>

The combination of DBD with the catalysts significantly enhanced

the CH<sub>4</sub> & CO<sub>2</sub> conversions and the production of syngas (Fig. 10), indicating the existence of plasma-assisted surface reactions in addition to the gas phase reactions. Compared to the plasma reaction without a catalyst, the presence of the catalyst in the plasma-catalytic DRM reaction induced the transition of the discharge mode, implicating an evolution from filamentary discharge to surface discharge. This phenomenon has been clearly shown in Fig. 6 and similar findings were also reported in previous works [31,52]. In the hybrid plasma-catalytic process, the plasma can enhance the activation of gas phase CH<sub>4</sub> & CO<sub>2</sub> and produce large amount of chemically reactive species including radicals, excited atoms, ions and molecules such as CO<sub>2</sub>(v), CO\*, CH<sub>3</sub>\*, CH<sub>2</sub>\*, CH\*, H\*, and O\* radicals. These energetic species are capable of initiating a range of gas phase and surface reactions. Another significant advantage of coupling a catalyst with a plasma system comes from the enhanced adsorption, namely, plasma-excited radicals in the boundary layer near the catalyst surfaces can be adsorbed directly, which may require a much lower energy to overcome energy barriers [53]. As a result, the reactions can take place between species adsorbed on the catalytic surface with either other adsorbed species or gas phase species near the catalyst surface. Clearly, more reaction channels for the DRM process could be initiated when placing the catalysts in the plasma, which significantly enhance the CH<sub>4</sub> & CO<sub>2</sub> conversions and the yield of products in the plasma-catalytic process.

The distinct catalytic performances between Ni/Al and Mo<sub>2</sub>C-Ni/Al catalysts were discussed here to understand the catalytic functions of Ni and Mo<sub>2</sub>C, respectively. As shown in Fig. 10, the conversions of CH<sub>4</sub> and CO<sub>2</sub> for Mo<sub>2</sub>C-Ni/Al-2 catalyst were higher (82.5% and 84.6%) compared with that of Ni/Al catalyst. A re-dispersion of Ni nanoparticles (8.2 nm → 5.3 nm) has been observed over the Mo<sub>2</sub>C-Ni/Al-2 catalyst due to the strong interaction between Ni and Mo<sub>2</sub>C. Ni nanoparticles with a smaller size favor the activation of CH<sub>4</sub> and CO<sub>2</sub> at higher rates, being consistent with other literatures [15,54]. As shown in Fig. 5, the addition of molybdenum carbide species can effectively promote the

adsorption and dissociation of CO<sub>2</sub>. And therefore the Mo<sub>2</sub>C-Ni/Al-2 catalyst showed better stability compared with Ni/Al reference. A bifunctional catalysis model can be reasonably established that the smaller Ni nanoparticle promotes the activation of CH<sub>4</sub> and the Mo<sub>2</sub>C facilitates CO<sub>2</sub> dissociation, achieving a matching rate of CH<sub>4</sub> activation and CO<sub>2</sub> dissociation via proper Ni/Mo molar ratio, and thereby a stable performance was maintained over the Mo<sub>2</sub>C-Ni/Al-2 catalyst. The characterization of the spent catalysts fully confirmed the above conclusions and the amount of coke deposited on the spent Ni/Al catalyst was obviously higher than that on Mo<sub>2</sub>C-Ni/Al-2 catalyst.

#### 4. Conclusions

Non-thermal plasma (NTP) coupled with catalysis enables the dry reforming of methane (DRM) reaction to occur without external heating, while the faster rate of CH<sub>4</sub> conversion than that of CO<sub>2</sub> brings the issues of coke deposition. Herein, β-Mo<sub>2</sub>C was employed as an effective component to activate CO<sub>2</sub> and Mo<sub>2</sub>C-Ni/Al series catalysts have been fabricated via mechanical mixing method with the optimal molar ratio of Ni/Mo (2/1) being used for the plasma-catalytic DRM reaction. The catalytic function of Mo<sub>2</sub>C-Ni/Al-2 catalyst enhanced with higher input powers, a matching conversion rate of CH<sub>4</sub> with that of CO<sub>2</sub> was obtained at the discharge power of 79 W, with CH<sub>4</sub> and CO<sub>2</sub> conversions higher than 80%, being kept stable during the tested hours without any extra-thermal input. The crucial roles of β-Mo<sub>2</sub>C additives in the plasma-assisted catalysis of DRM reaction were revealed in terms of facilitating the charge deposition, re-dispersion of Ni NPs over β-Mo<sub>2</sub>C and activation of CO<sub>2</sub>. Benefiting both from CO<sub>2</sub> dissociation catalyzed by β-Mo<sub>2</sub>C and the better Ni dispersion to active CH<sub>4</sub>, the Mo<sub>2</sub>C-Ni/Al<sub>2</sub>O<sub>3</sub> catalyst exhibited much better activity and stability as compared with the undoped Ni/Al<sub>2</sub>O<sub>3</sub> catalyst.

#### CRedit authorship contribution statement

**Yanan Diao:** Investigation, Methodology, Data curation, Writing – original draft, Software, Writing – review & editing. **Xiao Zhang:** Data curation, Methodology, Software, Writing – review & editing. **Yang Liu:** Data curation, Writing – review & editing. **Bingbing Chen:** Data curation, Writing – review & editing. **Guohao Wu:** Writing – review & editing. **Chuan Shi:** Writing – review & editing, Funding acquisition, Supervision, Project administration.

#### Declaration of Competing Interest

The authors declare that they have no known competing financial interests or personal relationships that could have appeared to influence the work reported in this paper.

#### Acknowledgment

The work was supported by the National Key R&D Program of China (No. 2017YFA0700103), the National Natural Science Foundation of China (Nos. 21872014, 21932002 and 21902018), the Liaoning Revitalization Talent Program (XLYC2008032) and the Fundamental Research Funds for the Central Universities (DUT20ZD205 and DUT21RC(3)095).

#### Appendix A. Supporting information

Supplementary data associated with this article can be found in the online version at [doi:10.1016/j.apcatb.2021.120779](https://doi.org/10.1016/j.apcatb.2021.120779).

#### References

- [1] D. Pakhare, J. Spivey, A review of dry (CO<sub>2</sub>) reforming of methane over noble metal catalysts, *Chem. Soc. Rev.* 43 (2014) 7813–7837.

- [2] Y. Wang, L. Yao, S. Wang, D. Mao, C. Hu, Low-temperature catalytic CO<sub>2</sub> dry reforming of methane on Ni-based catalysts: a review, *Fuel Process. Technol.* 169 (2018) 199–206.
- [3] X. Yan, T. Hu, P. Liu, S. Li, B. Zhao, Q. Zhang, W. Jiao, S. Chen, P. Wang, J. Lu, L. Fan, X. Deng, Y.-X. Pan, Highly efficient and stable Ni/CeO<sub>2</sub>-SiO<sub>2</sub> catalyst for dry reforming of methane: effect of interfacial structure of Ni/CeO<sub>2</sub> on SiO<sub>2</sub>, *Appl. Catal. B: Environ.* 246 (2019) 221–231.
- [4] M. Tang, K. Liu, D.M. Roddick, M. Fan, Enhanced lattice oxygen reactivity over Fe<sub>2</sub>O<sub>3</sub>/Al<sub>2</sub>O<sub>3</sub> redox catalyst for chemical-looping dry (CO<sub>2</sub>) reforming of CH<sub>4</sub>: synergistic La-Ce effect, *J. Catal.* 368 (2018) 38–52.
- [5] K. Sheng, D. Luan, H. Jiang, F. Zeng, B. Wei, F. Pang, J. Ge, NiCoY nanocatalyst supported by ZrO<sub>2</sub> hollow sphere for dry reforming of methane: synergetic catalysis by Ni and Co in alloy, *ACS Appl. Mater. Inter.* 11 (2019) 24078–24087.
- [6] S. Li, J. Gong, Strategies for improving the performance and stability of Ni-based catalysts for reforming reactions, *Chem. Soc. Rev.* 43 (2014) 7245–7256.
- [7] D. Li, V. Rohani, F. Fabry, A. Parakkulam Ramaswamy, M. Sennour, L. Fulcheri, Pyridinic nitrogen exclusively doped carbon materials as efficient oxygen reduction electrocatalysts for Zn-air batteries, *Appl. Catal. B: Environ.* 261 (2020) 118–228.
- [8] Y. Zeng, X. Zhu, D. Mei, B. Ashford, X. Tu, Plasma-catalytic dry reforming of methane over γ-Al<sub>2</sub>O<sub>3</sub> supported metal catalysts, *Catal. Today* 256 (2015) 80–87.
- [9] X. Tu, J.C. Whitehead, Crystal structure of the globular domain of C1QTNF5: implications for late-onset retinal macular degeneration, *Appl. Catal. B: Environ.* 125 (2012) 439–448.
- [10] S. Mahammadunnisa, P. Manoj Kumar Reddy, B. Ramaraju, C. Subrahmanyam, Catalytic nonthermal plasma reactor for dry reforming of methane, *Energy* 72 (2013) 4441–4447.
- [11] Q. Wang, Y. Cheng, Y. Jin, Dry reforming of methane in an atmospheric pressure plasma fluidized bed with Ni/γ-Al<sub>2</sub>O<sub>3</sub> catalyst, *Catal. Today* 148 (2009) 275–282.
- [12] J. Kim, M.S. Abbott, D.B. Go, J.C. Hicks, Enhancing C–H bond activation of methane via temperature-controlled, catalyst–plasma interactions, *ACS Energy Lett.* 1 (2016) 94–99.
- [13] D. Mei, B. Ashford, Y.-L. He, X. Tu, Plasma-catalytic reforming of biogas over supported Ni catalysts in a dielectric barrier discharge reactor: effect of catalyst supports, *Plasma Process. Polym.* 14 (2017) 1–13.
- [14] Y.X. Zeng, L. Wang, C.F. Wu, J.Q. Wang, B.X. Shen, X. Tu, Low temperature reforming of biogas over K-, Mg- and Ce-promoted Ni/Al<sub>2</sub>O<sub>3</sub> catalysts for the production of hydrogen rich syngas: understanding the plasma-catalytic synergy, *Appl. Catal. B: Environ.* 224 (2018) 469–478.
- [15] N. Wang, K. Shen, L. Huang, X. Yu, W. Qian, W. Chu, Facile route for synthesizing ordered mesoporous Ni–Ce–Al oxide materials and their catalytic performance for methane dry reforming to hydrogen and syngas, *ACS Catal.* 3 (2013) 1638–1651.
- [16] D. Li, R. Li, M. Lu, X. Lin, Y. Zhan, L. Jiang, Carbon dioxide reforming of methane over Ru catalysts supported on Mg–Al oxides: a highly dispersed and stable Ru/Mg (Al)O catalyst, *Appl. Catal. B: Environ.* 200 (2017) 566–577.
- [17] M. Zhang, J. Zhang, Z. Zhou, S. Chen, T. Zhang, F. Song, Q. Zhang, N. Tsubaki, Y. Tan, Y. Han, Effects of the surface adsorbed oxygen species tuned by rare-earth metal doping on dry reforming of methane over Ni/ZrO<sub>2</sub> catalyst, *Appl. Catal. B: Environ.* 264 (2020), 118522.
- [18] D. Yap, J.-M. Tatibouët, C. Batiot-Dupeyrat, Catalyst assisted by non-thermal plasma in dry reforming of methane at low temperature, *Catal. Today* 299 (2018) 263–271.
- [19] X. Zheng, S. Tan, L. Dong, S. Li, H. Chen, LaNiO<sub>3</sub>@SiO<sub>2</sub> core-shell nano-particles for the dry reforming of CH<sub>4</sub> in the dielectric barrier discharge plasma, *Int. J. Hydrog. Energ.* 39 (2014) 11360–11367.
- [20] X. Zhang, X. Zhu, L. Lin, S. Yao, M. Zhang, X. Liu, X. Wang, Y.-W. Li, C. Shi, D. Ma, Highly dispersed copper over β-Mo<sub>2</sub>C as an efficient and stable catalyst for the reverse water gas shift (RWGS) reaction, *ACS Catal.* 7 (2016) 912–918.
- [21] S. Zhang, C. Shi, B. Chen, Y. Zhang, Y. Zhu, J. Qiu, C. Au, Catalytic role of β-Mo<sub>2</sub>C in DRM catalysts that contain Ni and Mo, *Catal. Today* 258 (2015) 676–683.
- [22] X. Zhang, Y. Liu, M. Zhang, T. Yu, B. Chen, Y. Xu, M. Crocker, X. Zhu, Y. Zhu, R. Wang, D. Xiao, M. Bi, D. Ma, C. Shi, Synergy between β-Mo<sub>2</sub>C nanorods and non-thermal plasma for selective CO<sub>2</sub> reduction to CO, *Chem* 6 (2020) 3312–3328.
- [23] S. Yao, X. Zhang, W. Zhou, R. Gao, W. Xu, Y. Ye, L. Lin, X. Wen, P. Liu, B. Chen, E. Crumlin, J. Guo, Z. Zuo, W. Li, J. Xie, L. Lu, C.J. Kiely, L. Gu, C. Shi, J. A. Rodriguez, D. Ma, Atomic-layered Au clusters on α-MoC as catalysts for the low-temperature water-gas shift reaction, *Science* 357 (2017) 389–393.
- [24] L. Lin, W. Zhou, R. Gao, S. Yao, X. Zhang, W. Xu, S. Zheng, Z. Jiang, Q. Yu, Y.W. Li, C. Shi, X.D. Wen, D. Ma, Low-temperature hydrogen production from water and methanol using Pt/α-MoC catalysts, *Nature* 544 (2017) 80–83.
- [25] M. Danielis, S. Colussi, C. de Leitenburg, L. Soler, J. Llorca, A. Trovarelli, Outstanding methane oxidation performance of palladium-embedded ceria catalysts prepared by a one-step dry ball-milling method, *Angew. Chem. Int. Ed.* 57 (2018) 10212–10216.
- [26] T. Huang, Q. Peng, W. Shi, J. Xu, Y. Fan, An anionic surfactant-assisted equilibrium adsorption method to prepare highly dispersed Fe-promoted Ni/Al<sub>2</sub>O<sub>3</sub> catalysts for highly selective mercaptan removal, *Appl. Catal. B: Environ.* 230 (2018) 154–164.
- [27] F. Meng, X. Li, M. Li, X. Cui, Z. Li, Catalytic performance of CO methanation over La-promoted Ni/Al<sub>2</sub>O<sub>3</sub> catalyst in a slurry-bed reactor, *Chem. Eng. J.* 313 (2017) 1548–1555.
- [28] H. Zhang, Z. Luo, Y. Liu, Y. Jiang, Rational electronic control of carbon dioxide reduction over cobalt oxide, *Appl. Catal. B: Environ.* 277 (2020) 119–166.
- [29] N. Perret, X. Wang, L. Delannoy, C. Potvin, C. Louis, M.A. Keane, Enhanced selective nitroarene hydrogenation over Au supported on β-Mo<sub>2</sub>C and β-Mo<sub>2</sub>C/Al<sub>2</sub>O<sub>3</sub>, *J. Catal.* 286 (2012) 172–183.
- [30] L. Lin, Q. Yu, M. Peng, A. Li, S. Yao, S. Tian, X. Liu, A. Li, Z. Jiang, R. Gao, X. Han, Y.W. Li, X.D. Wen, W. Zhou, D. Ma, Atomically dispersed Ni/α-MoC catalyst for



- hydrogen production from methanol/water, *J. Am. Chem. Soc.* 143 (2021) 309–317.
- [31] X. Tu, H.J. Gallon, M.V. Twigg, P.A. Gorry, J.C. Whitehead, Dry reforming of methane over a Ni/Al<sub>2</sub>O<sub>3</sub> catalyst in a coaxial dielectric barrier discharge reactor, *J. Phys. D: Appl. Phys.* 44 (2011), 274007.
- [32] J. Li, Q.-Q. Yang, Y.-X. Hu, M.-C. Liu, C. Lu, H. Zhang, L.-B. Kong, W.-W. Liu, W.-J. Niu, K. Zhao, Y.-C. Wang, F. Cheng, Z.M. Wang, Y.-L. Chueh, Design of lamellar Mo<sub>2</sub>C nanosheets assembled by Mo<sub>2</sub>C nanoparticles as an anode material toward excellent sodium-ion capacitors, *ACS Sustain. Chem. Eng.* 7 (2019) 18375–18383.
- [33] J. Chen, C. Chen, Y. Chen, H. Wang, S. Mao, Y. Wang, Improving alkaline hydrogen evolution reaction kinetics on molybdenum carbide: Introducing Ru dopant, *J. Catal.* 392 (2020) 313–321.
- [34] R. Ge, J. Huo, M. Sun, M. Zhu, Y. Li, S. Chou, W. Li, Surface and Interface Engineering: Molybdenum Carbide-Based Nanomaterials for Electrochemical Energy Conversion, *Small* (2019), 1903380.
- [35] D. Ray, P.M.K. Reddy, C. Subrahmanyam, Ni-Mn/ $\gamma$ -Al<sub>2</sub>O<sub>3</sub> assisted plasma dry reforming of methane, *Catal. Today* 309 (2018) 212–218.
- [36] M. Yu, K. Zhu, Z. Liu, H. Xiao, W. Deng, X. Zhou, Carbon dioxide reforming of methane over promoted Ni<sub>x</sub>Mg<sub>1-x</sub>O (111) platelet catalyst derived from solvothermal synthesis, *Appl. Catal. B: Environ.* 148–149 (2014) 177–190.
- [37] W. Fang, S. Paul, M. Capron, F. Dumeignil, L. Jalowiecki-Duhamel, Hydrogen production from bioethanol catalyzed by Ni<sub>x</sub>Mg<sub>2</sub>AlO<sub>y</sub> ex-hydrotalcite catalysts, *Appl. Catal. B: Environ.* 152–153 (2014) 370–382.
- [38] H. Wu, G. Pantaleo, V. La Parola, A.M. Venezia, X. Collard, C. Aprile, L.F. Liotta, Bi- and trimetallic Ni catalysts over Al<sub>2</sub>O<sub>3</sub> and Al<sub>2</sub>O<sub>3</sub>-MO (M = Ce or Mg) oxides for methane dry reforming: Au and Pt additive effects, *Appl. Catal. B: Environ.* 156–157 (2014) 350–361.
- [39] M. Zhu, Y. Song, S. Chen, M. Li, L. Zhang, W. Xiang, Chemical looping dry reforming of methane with hydrogen generation on Fe<sub>2</sub>O<sub>3</sub>/Al<sub>2</sub>O<sub>3</sub> oxygen carrier, *Chem. Eng. J.* 368 (2019) 812–823.
- [40] S. Das, M. Sengupta, A. Bag, M. Shah, A. Bordoloi, Facile synthesis of highly disperse Ni-Co nanoparticles over mesoporous silica for enhanced methane dry reforming, *Nanoscale* 10 (2018) 6409–6425.
- [41] P. Wang, E. Tanabeb, J.J.K. Itob, H. Moriokab, T. Shishidoc, K. Takehira c, Filamentous carbon prepared by the catalytic pyrolysis of CH<sub>4</sub> on Ni/SiO<sub>2</sub>, *Appl. Catal. A: Gen.* 231 (2002) 35–44.
- [42] T. Stroud, T.J. Smith, E. Le Saché, J.L. Santos, M.A. Centeno, H. Arellano-Garcia, J. A. Odriozola, T.R. Reina, Chemical CO<sub>2</sub> recycling via dry and bi reforming of methane using Ni-Sn/Al<sub>2</sub>O<sub>3</sub> and Ni-Sn/CeO<sub>2</sub>-Al<sub>2</sub>O<sub>3</sub> catalysts, *Appl. Catal. B: Environ.* 224 (2018) 125–135.
- [43] R. Vakili, R. Gholami, C.E. Stere, S. Chansai, H. Chen, S.M. Holmes, Y. Jiao, C. Hardacre, X. Fan, Plasma-assisted catalytic dry reforming of methane (DRM) over metal-organic frameworks (MOFs)-based catalysts, *Appl. Catal. B: Environ.* 260 (2020) 118–195.
- [44] C. De Bie, B. Verheyde, T. Martens, J. van Dijk, S. Paulussen, A. Bogaerts, Fluid modeling of the conversion of methane into higher hydrocarbons in an atmospheric pressure dielectric barrier discharge: fluid modeling of the conversion of methane, *Plasma Process. Polym.* 8 (2011) 1033–1058.
- [45] H.J. Gallon, X. Tu, M.V. Twigg, J.C. Whitehead, Plasma-assisted methane reduction of a NiO catalyst—low temperature activation of methane and formation of carbon nanofibres, *Appl. Catal. B: Environ.* 106 (2011) 616–620.
- [46] A.H. Khoja, M. Tahir, N.A.S. Amin, Cold plasma dielectric barrier discharge reactor for dry reforming of methane over Ni/ $\gamma$ -Al<sub>2</sub>O<sub>3</sub>-MgO nanocomposite, *Fuel Process. Technol.* 178 (2018) 166–179.
- [47] Y. Li, C.-J. Liu, B. Eliasson, Y. Wang, Synthesis of oxygenates and higher hydrocarbons directly from methane and carbon dioxide using dielectric-barrier discharges: product distribution, *Energ. Fuel* 16 (2002) 864–870.
- [48] D. Mei, Y.-L. He, S. Liu, J. Yan, X. Tu, Optimization of CO<sub>2</sub> conversion in a cylindrical dielectric barrier discharge reactor using design of experiments: optimization of CO<sub>2</sub> conversion, *Plasma Process. Polym.* 13 (2016) 544–556.
- [49] A. Fridman, *Plasma Chemistry*, Cambridge University Press, New York, 2008.
- [50] H.C. Straub, D. Lin, B.G. Lindsay, K.A. Smith, R.F. Stebbings, Absolute partial cross sections for electron-impact ionization of CH<sub>4</sub> from threshold to 1000 eV, *J. Chem. Phys.* 106 (1997) 4430–4435.
- [51] Y. Itikawa, Cross sections for electron collisions with carbon dioxide, *J. Phys. Chem. Ref. Data* 31 (2002) 749–767.
- [52] D. Mei, X. Zhu, Y.-L. He, J.D. Yan, X. Tu, Plasma-assisted conversion of CO<sub>2</sub> in a dielectric barrier discharge reactor: understanding the effect of packing materials, *Plasma Sources Sci. T.* 24 (2014), 015011.
- [53] S. Zhang, G.S. Oehrlein, From thermal catalysis to plasma catalysis: a review of surface processes and their characterizations, *J. Phys. D: Appl. Phys.* 54 (2021), 213001.
- [54] F. Wang, B. Han, L. Zhang, L. Xu, H. Yu, W. Shi, CO<sub>2</sub> reforming with methane over small-sized Ni@SiO<sub>2</sub> catalysts with unique features of sintering-free and low carbon, *Appl. Catal. B: Environ.* 235 (2018) 26–35.